A Finite Volume Method for Modeling Discontinuous Electrical Activation in Cardiac Tissue

Running head: Modeling Electrical Activation in Cardiac Tissue

Mark Trew, Ian Le Grice, Bruce Smaill, and Andrew Pullan
Bioengineering Institute, The University of Auckland, New Zealand

Correspondence to:

Mark Trew,
Bioengineering Institute,
Private Bag 92019,
Auckland New Zealand
Telephone: 64 9 373 7599 x 85114
Fax.: 64 9 367 7157
Email: m.trew@auckland.ac.nz

Abstract

This paper describes a finite volume method for modeling electrical activation in a sample of cardiac tissue using the bidomain equations. Microstructural features to the level of cleavage planes between sheets of myocardial fibres in the tissue are explicitly represented. The key features of this implementation compared to previous modeling are that it is designed to represent physical discontinuities with no volume in the intracellular domain and to provide linear systems of equations that are computationally efficient to construct and solve. Results obtained using this method highlight how the understanding of discontinuous activation in cardiac tissue can form a basis for better understanding defibrillation processes and experimental recordings.

Key Terms

Bidomain Equations, Numerical Simulation, Computational Efficiency, Tissue Microstructure, Cleavage Planes, Shock, Bipolar Stimulus, Activation Times.

1 Introduction

Most computer models of cardiac electrical activation have assumed that the myocardium is a continuum, and that activation propagates most rapidly in the direction of the local myofiber axis and with equal velocity in the plane transverse to it. These assumptions of structural continuity and electrical transverse isotropy are at odds with observations of myocardial architecture over a period of more than twenty years. Microscopic studies[3, 23] have shown that ventricular myocytes are arranged in discrete bundles separated by cleavage planes or collagenous septae. It has also been demonstrated that ventricular myocardium should be viewed as an ordered network of interconnected muscle layers[23, 7, 12, 18] that have a predominantly radial orientation in apex-base transmural sections.[7, 12, 18, 41, 4]

There is strong evidence that discontinous myocyte organization significantly affects propagation velocity and the safety of conduction in two-dimensional tissue preparations.[30, 25, 16] Moreover, it acknowledged that defibrillating shocks would not produce cardioversion if the myocardium behaved as a continuum and structural discontinuity has also been evoked to explain the myocardial response to high voltage shocks.[15, 37, 6, 38, 20] These issues were addressed in a computational study in which a bidomain model of electrical propagation was solved in a discontinuous domain that accurately represented the transmural microstructure of the left ventricular free wall.[11] It was concluded that the laminar architecture of the myocardium would give rise to orthotropic electrical properties uniquely determined by local microstructure, and that interlaminar clefts between layers of myocytes could provide a substrate for bulk activation of the ventricles during defibrillation.

A number of limitations can be identified in relation to the finite element based modeling study presented by Hooks and co-workers.[11] The simulation was carried out using a tissue segment of relatively small dimensions. In order to investigate the extent to which structural discontinuity may contribute to re-entrant electrical activation it will be necessary to solve a full ionic current model in an extended discontinuous domain. This would impose substantial computational overheads if the finite element formulation used initially were to be preserved. A further concern is that this formulation potentially overstates the volume occupied by cleavage planes and it is uncertain whether this impacts on the results that have been obtained using this method.

Finite volume methods have been developed and used by Harrild et al.[8, 9] and Penland et al.[21] to solve the bidomain equations in complex three dimensional structures. In this paper we report on the development of a new finite volume method for modeling electrical activation in discontinuous cardiac tissue.

The finite volume paradigm in the context of explicit modeling of cleavage planes will be shown to have an advantage over the previously used finite element formuation in that cleavage planes can be represented as no-volume entities in the finite volume discretisation. A finite volume formulation also allows the resistance of the intercellular clefts to intracellular current flux to be varied. The method developed here has computational advantages over a traditional finite element method and other finite volume methods when modeling anisotropic conduction of electrical activation. The utility of this new finite volume approach has been assessed by comparing modeling results with those already obtained by Hooks and colleagues[11] using the finite element method and Buist and colleagues[2] using a finite difference based method. This provides an objective basis for vali-

dating results obtained using both approaches and for quantifying the advantages of the finite volume method.

2 Methods

2.1 Continuous and Discrete Forms of the Bidomain Equations

The bidomain model is conceptualised as two co-existent intracellular and extracellular domains.[10] The potential in the intracellular domain is denoted as ϕ_i and the potential in the extracellular domain is denoted as ϕ_e. The transmembrane potential difference, V_m, is given by:

$$V_m = \phi_i - \phi_e. \tag{1}$$

It is assumed that there are negligible capacitive, inductive and electromagnetic propagative effects within each of the two domains. The current across the membrane separating the domains is comprised of an ionic current flux, I_{ion}, a capacitive component including the rate of change of the transmembrane potential and a transmembrane stimulation current flux, I_m. The transmembrane stimulation current flux represents an intracellular anode and an extracellular cathode and so is a depolarising current flow across the membrane into the intracellular domain. Assuming that the currents obey Ohm's Law, conservation of current within the two domains leads to a system of two coupled reaction-diffusion equations. The intracellular potential variable may be eliminated in favour of the transmembrane potential dependent variable and the equations rearranged. This results in a coupled system comprised of a parabolic reaction-diffusion equation and an elliptic equation. These equations are referred to in their various forms as the bidomain

equations.[2]

$$A_m C_m \frac{\partial V_m}{\partial t} - \nabla \cdot (\boldsymbol{\sigma}_i \nabla V_m) = \nabla \cdot (\boldsymbol{\sigma}_i \nabla \phi_e) - A_m \left(I_{\text{ion}} - I_m\right) + i_i \qquad (2)$$

$$\nabla \cdot \left((\boldsymbol{\sigma}_e + \boldsymbol{\sigma}_i) \nabla \phi_e\right) = -\nabla \cdot (\boldsymbol{\sigma}_i \nabla V_m) - i_i - i_e \qquad (3)$$

A_m is the surface to volume ratio of the representative cell membrane between the domains and C_m is the specific membrane capacitance. $\boldsymbol{\sigma}_i$ and $\boldsymbol{\sigma}_e$ are the symmetric intra- and extra-cellular conductivity tensors respectively. These tensors may be anisotropic and spatially non-homogeneous. The terms i_i and i_e are current injections per unit volume into the intra- and extra-cellular spaces respectively. Equation (2) describes the conservation of current per unit volume in the intracellular domain and Eq. (3) describes the instantaneous distribution of current between the two domains. The bidomain equations are subject to intra- and extra-cellular potential flux boundary conditions.

It is assumed that there is no current flow from the intracellular domain to the extramyocardial domain. The boundary condition on the intracellular domain is thus:

$$\nabla \phi_i \cdot (\boldsymbol{\sigma}_i^T \boldsymbol{n}) = 0$$

$$\Rightarrow \ \nabla (V_m + \phi_e) \cdot (\boldsymbol{\sigma}_i \boldsymbol{n}) = 0. \qquad (4)$$

Note that the conductivity tensors are symmetric, *i.e.,* $\boldsymbol{\sigma}_i = \boldsymbol{\sigma}_i^T$. Current flow from the extracellular domain is matched by the extramyocardial domain so that the boundary condition on the extracellular domain is:

$$\nabla \phi_e \cdot (\boldsymbol{\sigma}_e \boldsymbol{n}) = \nabla \phi_o \cdot (\boldsymbol{\sigma}_o \boldsymbol{n}) \,. \qquad (5)$$

Here ϕ_o is an extramyocardial potential and $\boldsymbol{\sigma}_o$ is an extramyocardial conductivity. These values can represent a bath solution or the influence of a "torso". If neither of these regions is modeled the right hand side is zero.

Given a discretisation of the solution domain, Eq. (2) can be approximated by an algebraic system of ordinary differential equations in time and Eq. (3) by a stationary algebraic system, *i.e.*,

$$\boldsymbol{M}\frac{d\boldsymbol{V}_m(t)}{dt} - \boldsymbol{K}\boldsymbol{V}_m(t) = \boldsymbol{K}\boldsymbol{\phi}_e(t) + \boldsymbol{M}\left[-\frac{1}{C_m}\left(\boldsymbol{I}_{\text{ion}}(\boldsymbol{V}) - \boldsymbol{I}_m(t)\right)\right] + \boldsymbol{M}\left[\frac{1}{A_m C_m}\boldsymbol{i}_i(t)\right] \tag{6}$$

$$\boldsymbol{L}\boldsymbol{\phi}_e(t) = -\boldsymbol{K}\boldsymbol{V}(t) - \boldsymbol{M}\left[\frac{1}{A_m C_m}\left(\boldsymbol{i}_i(t) + \boldsymbol{i}_e(t)\right)\right]. \tag{7}$$

Here it is assumed that the capacitance of the membrane between the intra- and the extracellular domains is spatially homogeneous. The system $\boldsymbol{M}$ is commonly referred to as the mass matrix and the systems $\boldsymbol{K}$ and $\boldsymbol{L}$ are commonly referred to as the stiffness matrices. These systems have as many rows as there are finite volumes in the computational mesh. Mass and stiffness matrices for the bidomain equations have been constructed in previous studies using all of the classic spatial discretisation techniques such as finite difference methods,[17, 27, 29, 2] finite element methods,[11, 39, 33] finite volume methods[8, 9, 21] and collocation methods.[24] If excitation-contraction processes are not being modeled then the mass and stiffness matrices are stationary.

The system of ordinary differential equations given by Eq. (6) is integrated

over a discrete period of time from t^n to t^{n+1} to give:

$$\boldsymbol{M}\int_{t^n}^{t^{n+1}}\frac{d\boldsymbol{V}_m}{dt}dt-\boldsymbol{K}\int_{t^n}^{t^{n+1}}\boldsymbol{V}_m dt=$$
$$\boldsymbol{K}\int_{t^n}^{t^{n+1}}\boldsymbol{\phi}_e dt+\boldsymbol{M}\int_{t^n}^{t^{n+1}}-\frac{\boldsymbol{I}_{\text{ion}}-\boldsymbol{I}_m}{C_m}dt+\boldsymbol{M}\int_{t^n}^{t^{n+1}}\left[\frac{1}{A_m C_m}i_i(t)\right]dt. \quad (8)$$

An important issue in performing this temporal integration is that the time scale of the ionic membrane current processes, denoted by $\boldsymbol{I}_{\text{ion}}$, is much smaller than that of the intracellular diffusion processes. A fractional step operator splitting process[22, 42, 2] is used where an auxiliary problem for the membrane processes is solved first, followed by the intracellular diffusion problem.

The auxiliary term arises from:

$$\hat{\boldsymbol{V}}_m^{n+1}=\int_{t^n}^{t^{n+1}}-\frac{\boldsymbol{I}_{\text{ion}}-\boldsymbol{I}_m}{C_m}dt \quad (9)$$

where $\hat{\boldsymbol{V}}_m^{n+1}$ is a predictor membrane potential and $\hat{\boldsymbol{V}}_m^{n}=0$. The auxiliary equation that must be solved for the predictor membrane potential, $\hat{\boldsymbol{V}}_m$, is:

$$\frac{d\hat{\boldsymbol{V}}_m}{dt}=-\frac{\boldsymbol{I}_{\text{ion}}-\boldsymbol{I}_m}{C_m} \quad (10)$$

This equation may be solved using an ordinary differential equation solver appropriate to the nature of the cell model that will be used.[42, 34, 35] Not only does the time scale of the ionic membrane process as a whole differ greatly from the time scale of the intracellular diffusion process, but the time scales of the processes within the ionic membrane currents also differ widely. This is referred to as the stiffness of the system of ordinary differential equations.

The time integration of Eq. (8) can be performed in various ways. The results presented in this paper have been calculated using an identical split-step uncou-

pling to that of Buist et al.[2] For an implicit discretisation in time, the linear systems to be solved are:

$$(\boldsymbol{M} - \Delta t \boldsymbol{K})\, \boldsymbol{V}_m^{n+1} = \boldsymbol{M}\boldsymbol{V}_m^n + \Delta t \boldsymbol{K}\boldsymbol{\phi}_e^n + \Delta t \boldsymbol{M}\hat{\boldsymbol{V}}_m^{n+1} + \frac{\Delta t}{A_m C_m}\boldsymbol{M}\boldsymbol{i}_i(t) + \frac{\Delta t}{A_m C_m}\left[\boldsymbol{S}\left(\boldsymbol{V}_m^n\right) + \boldsymbol{S}\left(\boldsymbol{\phi}_e^n\right)\right] \quad (11)$$

$$\boldsymbol{L}\boldsymbol{\phi}_e^{n+1} = -\boldsymbol{K}\boldsymbol{V}_m^{n+1} - \frac{1}{A_m C_m}\boldsymbol{M}\left[\boldsymbol{i}_i(t) + \boldsymbol{i}_e(t)\right] - \frac{1}{A_m C_m}\left[\boldsymbol{S}_\phi\left(\boldsymbol{\phi}_e^n\right) + \boldsymbol{S}\left(\boldsymbol{V}_m^n\right)\right] \quad (12)$$

where $\boldsymbol{S}$ and $\boldsymbol{S}_\phi$ are vector sources representing the contributions from secondary current flux arising from fibre coordinates that are not oriented with the spatial discretisation.

An implicit temporal discretisation is chosen for Eqs. (11) and (12) to maintain a broad computational stability region. This is important since the computational meshes that are used must be highly resolved to represent the cleavage planes. This imposes a severe time step restriction if an explicit temporal discretisation is used. The resulting linear systems are solved using a preconditioned conjugate gradient method or generalised minimum residual method. The majority of the computational expense arises from the linear solution of Eq. (12). This Poisson equation with predominantly Neumann boundary conditions is poorly conditioned and it is both difficult and computationally expensive to construct a good preconditioner that significantly accelerates the iterative solution. Developing methods for improving the linear solution of Eq. (12) continues to be an ongoing field of research.

2.2 A Finite Volume Discretisation

We now introduce a finite volume method for constructing the stiffness and mass matrices. To derive the spatial discretisation we return to the bidomain equations given in Eqs. (2) and (3). The solution domain is formed from the union of unique non-interpenetrating finite volumes. The current conservation equations are enforced over each finite volume and hence over the entire solution domain. For a single finite volume, Ω_j, an integral expression of the bidomain equations, rearranged using the divergence theorem, is:

$$\int_{\Omega_j} A_m C_m \frac{\partial V_m}{\partial t} d\Omega - \int_{\Gamma_j} \nabla V_m \cdot (\boldsymbol{\sigma}_i \boldsymbol{n})\, d\Gamma = \int_{\Gamma_j} \nabla \phi_e \cdot (\boldsymbol{\sigma}_i \boldsymbol{n})\, d\Gamma - \int_{\Omega_j} (A_m (I_{\text{ion}} - I_m) + i_i)\, d\Omega \quad (13)$$

$$\int_{\Gamma_j} \nabla \phi_e \cdot ((\boldsymbol{\sigma}_e + \boldsymbol{\sigma}_i) \boldsymbol{n})\, d\Gamma = - \int_{\Gamma_j} \nabla V_m \cdot (\boldsymbol{\sigma}_i \boldsymbol{n})\, d\Gamma - \int_{\Omega_j} (i_i + i_e)\, d\Omega \quad (14)$$

where Γ_j is the boundary of Ω_j. These equations describe the balance of current fluxes through the finite volume faces, with current injected into or transferred through the membrane into the volume.

As is appropriate for the interpenetrating domains model of the bidomain equations, the intracellular and extracellular finite volumes share the same volume and faces. The volume of Ω_j is $\mathcal{V}_j$ and the boundary of the finite volume is expressed as a sum of discrete faces Γ_{jk}, each with area F_{jk}. A finite volume Ω_j has n_j faces internal to the domain and n_j^o faces external to the domain. The faces in intracellular, extracellular and extramyocardial space are weighted by W_{jk}^i, W_{jk}^e and W_{jk}^o respectively. These weights allow for the imposition of variable fluxes

from volume to volume. In the limiting case of an intracellular face representing a cleavage plane, $W^i_{jk} = 0$. External faces are subject to the boundary conditions given in Eqs. (4) and (5). Approximations to Eqs. (13) and (14) are thus given by:

$$A_{mj}C_{mj}\mathcal{V}_j\frac{dV_{mj}}{dt} - \sum_{k=1}^{n_j}(\nabla V_m)_{jk}\cdot(\boldsymbol{\sigma}_i\boldsymbol{n})_{jk}\,W^i_{jk}F_{jk}$$
$$= \sum_{k=1}^{n_j}(\nabla\phi_e)_{jk}\cdot(\boldsymbol{\sigma}_i\boldsymbol{n})_{jk}\,W^i_{jk}F_{jk} - \Big(A_{mj}\left(I_{\text{ion}} - I_m\right)_j + i_i\Big)\,\mathcal{V}_j \tag{15}$$

$$\sum_{k=1}^{n_j}(\nabla\phi_e)_{jk}\cdot\left(\left(W^e_{jk}\boldsymbol{\sigma}_e + W^i_{jk}\boldsymbol{\sigma}_i\right)\boldsymbol{n}\right)_{jk}F_{jk} + \sum_{k=1}^{n^o_j}(\nabla\phi_o)_{jk}\cdot(\boldsymbol{\sigma}_o\boldsymbol{n})_{jk}\,W^o_{jk}F_{jk} =$$
$$-\sum_{k=1}^{n_j}(\nabla V_m)_{jk}\cdot(\boldsymbol{\sigma}_i\boldsymbol{n})_{jk}\,W^i_{jk}F_{jk}\left(i_i - i_e\right)_j\mathcal{V}_j. \tag{16}$$

The finite volume discretisations used in evaluating Eqs. (15) and (16) are shown in Fig. 1(a).

[Figure 1 near here.]

2.3 Secondary Current Flux

Integrals over the finite volume faces can be expressed as the sum of primary and secondary flux terms.[14] The primary flux is the current flux normal to the volume face and the secondary flux is the flux in the plane of the face. Fig. 1(b) shows a face normal vector, $\boldsymbol{n}$, the unit vector connecting two adjacent volume centroids, $\boldsymbol{v}$, and the two unit in-face vectors, $\boldsymbol{u}$ and $\boldsymbol{w} = \boldsymbol{u}\times\boldsymbol{n}$. The decomposition of a

generic flux term on the face Γ_{jk} is:

$$\nabla\phi \cdot (\boldsymbol{\sigma n}) = \alpha\nabla\phi \cdot \boldsymbol{v} + \beta\nabla\phi \cdot \boldsymbol{u} + \gamma\nabla\phi \cdot \boldsymbol{w}. \tag{17}$$

The final two terms are often referred to as the secondary flux and the first term as the primary flux. The secondary flux will be zero when $\boldsymbol{v}$ and $\boldsymbol{n}$ are coincident and $\boldsymbol{\sigma}$ has principal directions coincident with $\boldsymbol{n}$, $\boldsymbol{u}$ and $\boldsymbol{w}$. Practically, this condition is met when the computational mesh of finite volumes is orthogonal and the cardiac muscle fibers are oriented along the mesh coordinate directions, or when the mesh is curvilinearly oriented along the fibers. Hence, secondary flux on the internal faces of volumes must be accounted for in orthogonal grids if the fibre field is not aligned with the coordinate directions and the conductivity is anisotropic. This is usually the case in practice.

The weights on the primary and secondary flux are determined by vector algebra as:

$$\alpha = \frac{(\sigma\boldsymbol{n}) \cdot \boldsymbol{n}}{\boldsymbol{v} \cdot \boldsymbol{n}} \tag{18}$$

$$\beta = (\sigma\boldsymbol{n}) \cdot \boldsymbol{u} - (\sigma\boldsymbol{n}) \cdot \boldsymbol{n}\frac{\boldsymbol{v} \cdot \boldsymbol{u}}{\boldsymbol{v} \cdot \boldsymbol{n}} \tag{19}$$

$$\gamma = (\sigma\boldsymbol{n}) \cdot \boldsymbol{w} - (\sigma\boldsymbol{n}) \cdot \boldsymbol{n}\frac{\boldsymbol{v} \cdot \boldsymbol{w}}{\boldsymbol{v} \cdot \boldsymbol{n}}. \tag{20}$$

If the distance between the centroids of the finite volumes Ω_j and Ω_k (lying on the opposite side of the jk face) is Δ_{jk}, then the flux term can be approximated as:

$$\nabla\phi \cdot (\sigma\boldsymbol{n}) = \alpha\frac{(\phi_k - \phi_j)}{\Delta_{jk}} + \beta\nabla\phi \cdot \boldsymbol{u} + \gamma\nabla\phi \cdot \boldsymbol{w} \tag{21}$$

If the vectors $\boldsymbol{v}$ and $\boldsymbol{n}$ are coincident (as is the case for an orthogonal computa-

tional mesh), then the expression for primary and secondary flux becomes:

$$\nabla\phi \cdot (\sigma \boldsymbol{n}) = ((\sigma \boldsymbol{n}) \cdot \boldsymbol{n}) \frac{(\phi_k - \phi_j)}{\Delta} + ((\sigma \boldsymbol{n}) \cdot \boldsymbol{u})(\nabla\phi \cdot \boldsymbol{u}) + ((\sigma \boldsymbol{n}) \cdot \boldsymbol{w})(\nabla\phi \cdot \boldsymbol{w}) \tag{22}$$

The approximation of $\nabla\phi$ on the cell volume faces results in extra computational costs for non-orthogonal computational meshes. The applications of the finite volume method described is this paper are made on orthogonal meshes. Hence, second order finite differences are used to evaluate potential gradients at finite volume centres and these are linearly interpolated onto the finite volume faces. Fig. 2 shows examples of this.

[Figure 2 near here.]

When the mesh is not orthogonal there are a number of possible approaches to computing an approximation to $\nabla\phi$ on the finite volume faces. For example: radial basis functions (also used in mesh free methods[19]), least-squares gradient reconstruction (LSGR) (also used in mesh free methods[19] and generalised finite difference methods[36]), least-squares polynomial reconstruction (LSPR) and linear shape functions (LSF)[14] can all be used as interpolating functions for computing approximations to $\nabla\phi$ on non-orthogonal meshes.

The secondary flux functions are:

$$S_j\left(\boldsymbol{\phi}^n\right) = \sum_{k=1}^{n_j} w_{jk}^i F_{jk} \Big[\left(\left(\boldsymbol{\sigma}_i \boldsymbol{n}\right) \cdot \boldsymbol{u} \right)_{jk} \left(\nabla \phi^n \cdot \boldsymbol{u} \right)_{jk} + \left(\left(\boldsymbol{\sigma}_i \boldsymbol{n}\right) \cdot \boldsymbol{w} \right)_{jk} \left(\nabla \phi^n \cdot \boldsymbol{w} \right)_{jk} \Big] \tag{23}$$

$$S_{\phi_j}\left(\boldsymbol{\phi}^n\right) = \sum_{k=1}^{n_j} w_{jk}^e F_{jk} \Big[\left(\left(\boldsymbol{\sigma}_e \boldsymbol{n}\right) \cdot \boldsymbol{u} \right)_{jk} \left(\nabla \phi^n \cdot \boldsymbol{u} \right)_{jk} + \left(\left(\boldsymbol{\sigma}_e \boldsymbol{n}\right) \cdot \boldsymbol{w} \right)_{jk} \left(\nabla \phi^n \cdot \boldsymbol{w} \right)_{jk} \Big] + S_j\left(\boldsymbol{\phi}^n\right). \tag{24}$$

These contributions are added to Eqs. (11) and (12) as source terms.

2.4 Discrete Representations of Cleavage Planes

Cleavage planes, which are visible in fresh transmural segments of left-ventricular wall tissue (Fig. 3(a)) and even more visible in lightly fixed tissue, are clearly seen in the dehydrated embedded tissue required for three-dimensional imaging and reconstruction. The reconstructed images of dehydrated embedded tissue of Fig. 3(b) is part of the image set obtained by Young et al.[41]

[Figure 3 near here.]

A discrete representation of cleavage planes from the tissue sample of Fig. 3(b) has been obtained previously.[11] The planes were manually segmented from images slices and described as bilinear finite element patches. Measurements of fiber orientations were also made and their transmural variation described linearly. The bilinear finite element representations of the cleavage planes together with the fiber orientations are shown in Fig. 4(a).

For the work presented in this paper a simple algorithm was designed and implemented in computer code that determined which finite volume faces of a given finite volume mesh intersected the cleavage plane finite element representations. This process identified the finite volume cleavage faces. An example of the resulting discrete representation of the cleavage planes is shown in Fig. 4(b). This approach allowed discrete finite volume representations of cleavage planes to be easily constructed for varying mesh resolutions.

[Figure 4 near here.]

2.5 Tissue Models and Finite Volume Meshes

Structured, orthogonal finite volume meshes were used in the modeling described in this paper. As discussed earlier such meshes are desirable from a computational perspective. In addition, these meshes are amenable to automatic generation. The approach used in this research was identical to that described by Buist et al.[2] The geometry of the tissue was described by a finite element mesh and within each element a structured mesh of finite volumes was automatically generated. The tissue sample of Fig. 3(b) has a rectangular geometry so the resulting finite volume meshes were orthogonal.

Several models were constructed. The first two were used for the purpose of testing and validating the finite volume method and the remainder were used to consider the role of cleavage planes in the activation of discontinuous tissue.

2.5.1 Models for Testing Computational Performance and Validation

The finite volume method and a tri-linear finite element method identical to that described by Hooks et al.[11] were used to generate the linear systems of Eqs. (11)

and (12). The sparsity of these systems and the performance of a conjugate gradient solution for a test load vector was compared between the methods. The domain was a three-dimensional cube with equal mesh resolution along all axes. No ionic current models were defined and a test load vector with a L2 norm of one was used to drive the solution process. The minimum, mean and maximum CPU times required to perform 17 non-preconditioned iterations of a conjugate gradient solver on the finite volume and finite element systems were gathered from 12 solution runs for each level of mesh discretisation. Calculations were performed using one 1.3 GHz Power 4 processor on an IBM Regatta P690.

The second model was a two-dimensional $12\ mm \times 12\ mm$ sample of tissue with equal mesh discretisation in both directions. This model was used to compare conduction velocity in the fiber and cross fiber directions between the finite volume method, the finite element method[11] and the finite difference method as described by Buist et al.[2] The tissue was stimulated at the midpoint by a transmembrane current injection and the spreading activation wave modeled using the bidomain equations and a simple cubic ionic model.[13] The fibre direction was set to be at $45°$ to the horizontal over the entire domain. Anisotropic fiber and cross-fiber conductivities were specified in the intracellular space of $0.2\ mS\ mm^{-1}$ and $0.02\ mS\ mm^{-1}$ and in the extracellular space of $0.2\ mS\ mm^{-1}$ and $0.1\ mS\ mm^{-1}$ following previously suggested physiological ratios.[26] This fibre orientation was chosen to provide the most extreme test of the secondary flux calculations in the finite volume method. The local conduction speeds in the fibre and cross fibre directions were determined at two sample points where these directions were normal to the activation wavefront. The local conduction speeds were calculated by interpolation from the local activation time field, specified as the time of maxi-

mum upstroke gradient in the transmembrane potential. The problem set-up and sample point locations are shown in Fig. 6(b). Six levels of spatial discretisation from $1\ mm$ to $0.03125\ mm$ were defined and a time discretisation of $0.01\ ms$ was used.

2.5.2 Extracellular Shock Simulation Models

A three dimensional discontinuous model of the tissue sample of Fig. 3(b) was constructed using the bilinear finite element description of the cleavage planes projected onto the finite volume mesh. An indentical continuous model without cleavage planes was utilised for comparison. Both models were activated by a constant extracellular transmural potential gradient of $6.7\ V\ cm^{-1}$, *i.e.*, $2000\ mV$ across the $3.0\ mm$ sample, representing a shock stimulus. The Drouhard-Roberge modified[5] Beeler-Reuter[1] ionic current model with additional revisions[29] was used. Mesh boundary conditions were imposed that connected together computational points on opposing transmural faces, resulting in no explicit external transmural boundaries. This is shown in Fig. 5(a). This type of boundary condition was used to minimise the effects of sudden no-flux boundaries and was appropriate as the shock stimuli were applied over the entire epi- and endocardial faces.

A computational mesh with a resolution of $0.01\ mm$ in all directions was defined together with a time step of $0.005\ ms$. Both the discontinuous and continuous models utilised the same extracellular conductivities of 0.263, 0.1087 and $0.1087\ mS\ mm^{-1}$ in the fibre, sheet and sheet-normal directions respectively. The intracellular conductivities in the discontinuous model were specified as 0.263, 0.0263 and 0.0263 and those of the continuous model as 0.263, 0.0263 and 0.01 $mS\ mm^{-1}$ in the fibre, sheet and sheet-normal directions respectively. The low

sheet-normal value in the continuous model was chosen to implicitly represent cleavage plane influence and follows the value determined by Hooks et al.[11]

2.5.3 Extracellular Bipolar Midwall Stimulation Models

A bipolar extracellular midwall stimulus in the tissue sample of Fig. 3(b) was modeled using a mesh with $0.02\ mm$ resolution and a time step of $0.1\ ms$. The anode and cathode were placed adjacent on either side of the midwall plane. A cubic ionic current model was used. Solutions were generated in a discontinuous (with explicit cleavage planes) and a continuous (without cleavage planes) model with conductivities identical to those described for the shock models. The solution domain was padded with continuous tissue along the transmural faces as shown in Fig. 5(b). This padding removed the immediate boundary influence from the region of interest (the tissue sample being modeled) and placed it in the far-field. The mesh resolution was cubically graded in the padding region to minimise the number of unknowns.

[Figure 5 near here.]

3 Results

3.1 Validation of the Finite Volume Method and Computational Comparison with other Methods

The finite volume systems have approximately 75% fewer non-zero entries compared to the finite element system entries for a given mesh. Fig. 6(a) shows the comparative mean, minimum and maximum CPU times taken to perform the 17 non-preconditioned iterations of a conjugate gradient solver on the finite volume

and finite element systems.

[Figure 6 near here.]

The variation of conduction speed with mesh resolution in the two-dimensional model is shown in the fiber direction at sample point 1 in Fig. 6(c) and in the cross-fibre direction at sample point 2 in Fig. 6(d).

3.2 Extracellular Shock Stimulation

[Figure 7 near here.]

Aspects of solutions from the extracellular shock simulation models are shown in Figs. 7 and 8. In Fig. 7 transmembrane potential maps show depolarisation occuring on the anodal side of the cleavage planes. These sources lead to a more rapid transmural depolarisation compared to the continuous model. Also shown is the map of regions throughout the discontinuous model which exhibit an early onset of activation.

The centerline traces in Fig. 8 show solutions generated for discontinuous and continuous tissue models by the finite volume method and a finite element method at two different mesh resolutions. Also included are solutions generated using the finite volume method with a thickness of $0.01\ mm$ attributed to the cleavage planes.

[Figure 8 near here.]

3.3 Extracellular Bipolar Midwall Stimulation

Figs. 9(a) and 9(b) show the positions of the activation wavefront at a sequence of instances in time for the continuous and discontinuous bipolar stimulus models. Fig. 9(c) shows the activation time fields for the continuous and discontinuous solutions on a selection of transmural planes. Activation times above $10\ ms$ have been contoured.

4 Discussion

In this paper we have presented a finite volume method developed for large-scale bidomain modeling of electrical activation in cardiac tissue. Our principal goal has been to suppliment the finite element method previously used for this purpose[11] with a method that was computationally cheaper and in which the volume of physical discontinuities in the intracellular domain was not overstated. We have assessed the method through comparative solutions in an idealised test problem and by modeling similar problems in discontinuous domains to those performed previously.[11]

Our finite volume method is deliberately designed to be as simple and as efficient as possible. To this end, modelling is only undertaken in a rectangular block of tissue with an orthogonal, regular computational mesh. The method we present is extendible to non-orthogonal, arbitrary and unstructured meshes, albeit with an associated loss in computational performance due to additional geometric calculations and increased non-zero entries in each row of the linear system of discrete equations. The systems of equations can be easily constructed in parallel and the number of non-zero entries per row in the linear systems of equations are

small (≤ 7 in three-dimensions as opposed to traditional finite element[11] or recent bidomain finite volume[21] methods with up to 27 non-zero entries per row). Not only are these sparse matrices beneficial from the perspective of memory usage, but the inner products required to perform, for example, a conjugate gradient solution can be evaluated more efficiently. This is shown in Fig. 6(a). No distinction between the system arising from the parabolic Eq. (11) and the elliptic Eq. (12) is necessary since the test is looking at the inner product cost which is related to the sparsity pattern and this is identical for both systems in the absence of cleavage planes. The systems of equations arising from the finite difference method are not symmetric due to the explicit representation of Neumann boundary conditions.[2] Hence, they cannot be solved using the conjugate gradient method and other iterative methods must be used. Given that there are approximately 19 non-zero entries per row in the finite difference system of equations,[2] the curve representing CPU solution times for a symmetric system with an equivalent sparsity would lie between the finite volume and the finite element curves of Fig. 6(a). The emphasis on storage and computational efficiency has been motivated by the fact that the mesh resolution required to geometrically capture the cleavage planes is typically greater than what would be required to adequately cature activation wavefronts in continuous tissue.[10, 34]

The results of Fig. 6 show that the secondary flux approximations used by the finite volume method do not appear to be detrimental to its accuracy when modeling using physiological parameters. The finite element method with linear interpolation will have a smaller truncation error for a given mesh resolution compared to the lower order finite volume method and so will converge with discretisation faster (this can be observed in Figs. 6(c) and 6(d)). However, the rate

of increase of iterative solver cost is greater for the finite element method and at approximately 1.7 million degrees of freedom it is well over twice as expensive as the finite volume solutions. For the results shown in Fig. 7 there are over 1.9 million degrees of freedom in each system. The gains in computational performance of the finite volume method compared to other methods appear to outweigh any possible detrimental accuracy effects due to representing the secondary flux as explicit source terms.

The shock solutions of Fig. 7 reinforce the observations make by Hooks and co-workers.[11] Among the principal differences between the solutions and these finite volume solutions is that the tissue is not depolarised to the same extent in the region of the cleavage planes closest to the endocardial surface. A source of this difference may be elucidated from the spatial traces shown in Fig. 8. It can be observed that increasing the volume associated with the cleavage breaks in the finite volume solution results in the activation wave better resembling the finite element solution. In addition to the cleavage plane volume, the numerical boundary conditions applied to the shock stimulation model in this work differ from the previous work.

Recent experimental results provide evidence for transmural virtual source formation in a wedge preparation with transmurally applied shocks of a similar magnitude to those used in this work.[28] Although it is unclear what effect the cut surface will have on the formation of these virtual sources, the authors discuss the possibility that they arise due to microscopic discontinuities in the tissue structure.

We have presented bipolar extracellular stimulation results (Fig. 9) since this protocol is usually used in experiments undertaken in our laboratory. The gross characteristics of the activation wavefronts of the bipolar extracellular stimulation

differ only slightly between the continuous model and the discontinuous model as seen in Figs. 9(a) and 9(b). However, the maps of activation times for the discontinuous model clearly show regions of early activation surrounded by regions of later activation in Fig. 9(c). The xy-midplane maps (which are in the midwall fibre plane) of activation times show the virtual anodes associated with the stimulating cathode and the virtual cathodes associated with the stimulating anode. The classic dog-bone shape around the cathode and anode make stimulation regions is also observed, albeit more clearly in the continuous tissue case. Both these behaviors have been illustrated experimentally for unipolar stimulation.[40] The differences between the early and late activations in these isolated regions is around $5\ ms$. This time-frame for discontinuous activation could easily be registered by fortuitously placed extracellular electrodes in an experimental preparation sampling at $1\ kHz$. We have also generated solutions in a model with a transmembrane midwall stimulus similar to that presented in previous work.[11] These additional solutions show activation behavior away from the stimulus site that is almost identical to the bipolar results, including regions of isolated early activation. The combination of the bipolar extracellular stimulus results presented here and the transmembrane results further reinforce the conclusions of the studies of Hooks and co-workers.[11]

Our finite volume method has enabled us to solve larger problems more efficiently that had been the case with previous explicit cleavage plane bidomain activation modeling. Ongoing work in our laboratory is now considering questions of reentrant activation in larger tissue samples. This will require an extensive description of cardiac tissue structure in a much larger tissue sample than what has been used as the basis for the results presented here. We have also addressed the

modeling issue in previous work of non-negligible volume being attributed to the cleavage planes and introduced new capabilities in terms of boundary conditions. Ongoing work also includes investigating the feature of the model where the intracellular current flow across cleavage planes is modified from impermeable to fully permeable. Such modeling would enable studies of the validity of coarser models of cleavage planes to be carried out. It would also enable the investigation of the effects of small current leakage across cleavage planes, arising perhaps from inter-myocyte electric field interactions.[32, 31]

5 Conclusions

In this paper we have described a finite volume discretisation of the bidomain equations that has been designed to enable the modelling of a discontinuous intracellular domain, notably with the explicit inclusion of electrically non-conducting cleavage planes. The use of a method that does not assign volume to the cleavage planes has been shown to quantitatively affect the depolarisation of the discontinuous tissue under extreme extracellular potential gradients. The finite volume method, as presented here, had a lower computational cost compared to other methods and this made it amenable for solving the large systems of equations that resulted from the spatial resolution required to capture the essential features of the cleavage planes.

The results presented here added further modelling validation to the conclusions of Hooks et al.[11] that cleavage plane discontinuities were likely to contribute significantly to a discontinuous propagation of electrical activation. As such, the provide a mechanism for explaining the bulk activation of myocardium in the

presence of large extracellular potential gradients. Clearly this has important implications for the defibrillation of cardiac tissue.

Further work is being conducted to use the finite volume method described here for better understanding the implications of discontinuous activation for both normal and abnormal cardiac excitation. This includes modeling defibrillation in larger tissue samples where there are pre-existing reentrant activation waves.

6 Acknowledgements

The authors would like to acknowledge the Royal Society of New Zealand Marsden Fund for supporting this work.

References

[1] Beeler, G. and H.Reuter. Reconstruction of the action potential of ventricular myocardial fibers. *Journal of Physiology* 268:177–210, 1977.

[2] Buist, M., G. Sands, P. Hunter, and A. Pullan. A Deformable Finite Element Derived Finite Difference Method for Cardiac Activation Problems. *Annals of Biomedical Engineering* 31:577–588, 2003.

[3] Caulfield, J. and T. Borg. The collagen network of the heart. *Laboratory Investigation* 40:364–372, 1979.

[4] Costa, K., Y. Takayama, A. McCulloch, and J. Covell. Laminar fiber architecture and three-dimensional systolic mechanics in canine ventricular myocardium. *American Journal of Physiology* 276:H595–H607, 1999.

[5] Drouhard, J. and F. Roberge. A simulation study of the ventricular myocardial action potential. *IEEE Transactions on Biomedical Engineering* 29:494–502, 1982.

[6] Fast, V., S. Rohr, A. Gillis, and A. Kleber. Activation of cardiac tissue by extracellualr electrical shocks. Formation of 'secondary sources' at intercellular clefts in monolayers of cultured myocytes. *Circulation Research* 82:375–385, 1998.

[7] Feneis, H. Da gefüge des herzmuskels bei systole und diastole. *Morphologisches Jahrbuch* 89:371–406, 1943.

[8] Harrild, D. and C. Henriquez. A Finite Volume Model of Cardiac Propagation. *Annals of Biomedical Engineering* 25:315–334, 1997.

[9] Harrild, D., R. Penland, and C. Henriquez. A Flexible Method for Simulating Cardiac Conduction in Three-Dimensional Complex Geometries. *Journal of Electrocardiology* 33(3):241–251, 2000.

[10] Henriquez, C. Simulating the electrical behavior of cardiac tissue using the bidomain model. *Critical Reviews in Biomedical Engineering* 21:1–77, 1993.

[11] Hooks, D., K. Tomlinson, S. Marsden, I. LeGrice, B. Smaill, A. Pullan, and P. Hunter. Cardiac Microstructure: Implications for Electrical Propagation and Defibrillation in the Heart. *Circulation Research* 91(4):331–338, August 23 2002.

[12] Hort, W. Makroskopische und mikrometrische untersuchungen am myokard verschieden stark gefüllter linker kammern. *Virchows Archiv - An International Journal of Pathology* 333:523–564, 1960.

[13] Hunter, P., P. McNaughton, and D. Noble. Analytical models of propagation in excitable cells. *Progress in Biophysical and Molecular Biology* 30(2/3):99–144, 1975.

[14] Jayantha, P. and I. Turner. On the use of surface interpolation techniques in generalised finite volume strategies for simulating transport in highly anisotropic porous media. *Journal of Computational and Applied Mathematics* 152:199–216, 2003.

[15] Krassowska, W., D. Frazier, T. Pilkington, and R. Ideker. Potential distribution in three-dimensional periodic myocardium - Part II: application to extracellular stimulation. *IEEE Transactions on Biomedical Engineering* 37:267–284, 1990.

[16] Kucera, J., A. Kleber, and S. Rohr. Slow conduction in cardiac tissue, II. Effects of branching tissue geometry. *Circulation Research* 83:795–805, 1998.

[17] Latimer, D. and B. Roth. Electrical Stimulation of Cardiac Tissue by a Bipolar Electrode in a Conductive Bath. *IEEE Transactions on Biomedical Engineering* 45(12), December 1998.

[18] LeGrice, I., B. Smaill, L. Chai, S. Edgar, J. Gavin, and P. Hunter. Laminar structure of the heart: ventricular myocyte arrangement and connective tissue architecture in the dog. *American Journal of Physiology* 269:H571–H582, 1995.

[19] Liu, G. *Mesh free methods: moving beyond the finite element method*. CRC Press LLC, 2002. ISBN 0-8439-1238-8.

[20] Newton, J., S. Knisley, X. Zhou, A. Pollard, and R. Ideker. Review of mechanisms by which electrical stimulation alters the transmembrane potential. *Journal of Cardiovascular Electrophysiology* 10:234–243, 1999.

[21] Penland, R., D. Harrild, and C. Henriquez. Modeling impulse propagation and extracellular potential distributions in anisotropic cardiac tissue using a finite volume element discretization. *Computing and Visualization in Science* 4:215–226, 2002.

[22] Qu, Z. and A. Garfinkel. An Advanced Alogrithm for Solving Partial Differential Equation in Cardiac Conduction. *IEEE Transactions on Biomedical Engineering* 46(9):1166–1168, September 1999.

[23] Robinson, T., L. Cohen-Gould, and S. Factor. Skeletal framework of mammalian heart muscle. *Laboratory Investigation* 49:482–498, 1983.

[24] Rogers, J. and A. McCulloch. A Collocation-Galerkin Finite Element Model of Cardiac Action Potential Propagation. *IEEE Transactions on Biomedical Engineering* 41(8):743–757, August 1994.

[25] Rohr, S., J. Kucera, V. Fast, and A. Kleber. Paradoxical improvements of impulse conduction in cardiac tissue by partial cellular uncoupling. *Science* 275:841–844, 1997.

[26] Roth, B. Electrical conductivity values used with the bidomain model of cardiac tissue. *IEEE Transactions on Biomedical Engineering* 44(4):326–328, 1997.

[27] Saleheen, H. and K. Ng. A New Three-Dimensional Finite-Difference Bidomain Formulation for Inhomogeneous Anisotropic Cardiac Tissues. *IEEE Transactions on Biomedical Engineering* 45(1):15–25, 1998.

[28] Sharifov, O. and V. Fast. Optical Mapping of Transmural Activation Induced by Electrical Shocks in Isolated Left Ventricular Wall Wedge Preparations. *JCE* 14(11):1215–1222, November 2003.

[29] Skouibine, K., N. Trayanova, and P. Moore. A numerically efficient model for simulation of defibrillation in an active bidomain sheet of myocardium. *Mathematical Biosciences* 166:85–100, 2000.

[30] Spach, M. and P. Dolber. Relating Extracellular Potentials and Their Derivatives to Anisotropic Propagation at the Microscopic Level in Human Cardiac Muscle. *Circulation Research* 58(3):356–371, March 1996.

[31] Sperelakis, N. An Electric Field Mechanism for Transmission of Excitation Between Myocardial Cells. *Circulation Research* 91:985–987, 2002.

[32] Sperelakis, N. and K. McConnell. Electric Field Interactions Between Closely Abutting Excitable Cells. *IEEE Engineering in Medicine and Biology* 21(1):77–89, January/February 2002.

[33] Sundnes, J., G. Lines, K. Mardal, and A. Tveito. Multigrid block preconditioning for a coupled system of partial differential equations modeling the electrical activity in the heart. *Computer Methods in Biomechanics and Biomedical Engineering* 5(6):397–409, 2002.

[34] Sundnes, J., G. Lines, and A. Tveito. Efficient solution of ordinary differential equations modeling electrical activity in cardiac cells. *Mathematical Biosciences* 172:55–72, 2001.

[35] Sundnes, J., G. Lines, and A. Tveito. ODE Solvers for a Stiff System Arising in the Modeling of the Electrical Activity of the Heart. *International Journal of Nonlinear Sciences and Numerical Simulation* 3(3), 2002.

[36] Tang, D., C. Yang, S. Kobayashi, and D. Ku. Generalised finite difference method for 3-D viscous flow in stenotic tubes with large wall deformation and collapse. *Applied Numerical Mathematics* 38:49–68, 2001.

[37] Trayanova, N. Discrete versus syncytial tissue behavior in a model of cardiac stimulation - II: Results of simulation. *IEEE Transactions on Biomedical Engineering* 43:1141–1150, 1996.

[38] Trayanova, N. Far-field stimulation of cardiac tissue. *Herzschr Elektrophys* 10:137–148, 1999.

[39] Vigmond, E., F. Anguel, and N. Trayanova. Computational Techniques for Solving the Bidomain Equations in Three Dimensions. *IEEE Transactions on Biomedical Engineering* 49(1):1260–1269, November 2002.

[40] Wikswo, Jr., J., S. Lin, and R. Abbas. Virtual Electrodes in Cardiac Tissue: A Common Mechanism for Anodal and Cathodal Stimulation. *Biophysical Journal* 69:2195–2210, December 1995.

[41] Young, A., I. LeGrice, M. Young, and B. Smaill. Extended confocal microscopy of myocardial laminae and collagen network. *Journal of Microscopy* 192(2):139–150, November 1998.

[42] Yung, C. *Application of a Stiff, Operator-Splitting Scheme to the Computational Modeling of Electrical Propagation in Cardiac Ventricles*. Master's thesis, Johns Hopkins University, Baltimore, Maryland, December 2000. Master of Science in Engineering.

Figure Legends

Fig. 1 A finite volume mesh and components. (a) A volume j within the finite volume mesh. The lower face is a no-flux intracellular face modelling a cleavage plane. An adjacent volume to the right is denoted as volume k. (b) Primary and secondary flux through a finite volume face. The primary flux is normal to the face and the secondary flux lies in the plane of the face. $\boldsymbol{u}$ and $\boldsymbol{w}$ are two in-face vectors that are orthogonal to each other and the vector normal to the face, $\boldsymbol{n}$. In the results presented in this paper, $\boldsymbol{v}$ is coincident to $\boldsymbol{n}$ and the secondary flux arises due to the anisotropy of the intra- and extra-cellular conductivities.

Fig. 2 Finite difference templates for computing derivative approximations for secondary flux calculations on an orthogonal finite volume mesh. (a) Standard second-order finite difference approximations for a finite volume with full flux intracellular faces. (b) Second order finite difference approximations for a finite volume with a no-flux intracellular face.

Fig. 3 Illustrations of cleavage planes between sheets of cardiac myocytes. (a) Porcine cardiac left-ventricular tissue that has been perfusion fixed with formalin and stained by brushing the surface with Evans blue dye. (b) A confocal microscope scan of dried and resin embedded rat cardiac left-ventricular tissue in two- and three-dimensional views. Further details may be found in LeGrice et al.[18] The physical dimensions of the sample are $3\ mm \times 0.8\ mm \times 0.8\ mm$.

Fig. 4 Discrete representations of cleavage planes. (a) The segmented cleavage breaks and fibre and sheet directions of the block of rat cardiac tissue shown in Fig. 3(b). The cleavage breaks are represented as bilinear surfaces. (b) The cleavage planes projected onto an orthogonal finite volume mesh.

Fig. 5 Finite volume meshes. (a) Continuous boundary wrapping on a regular mesh. (b) An example of the mesh grading used to extend the rat cardiac tissue sample. This view is of the epicardial face.

Fig. 6 Finite volume method validation and timing results. (a) Mean CPU times, over 12 samples, required to perform 17 unpreconditioned steps of a conjugate gradient solver on the systems arising from finite element and finite volume discretisations of the bidomain equations. Error bars indicate the minimum and maximum CPU times. (b-d) Validation results comparing the convergence of derived conduction speeds in fibre and cross fibre directions at two sample points for finite element, finite volume and finite difference methods.

Fig. 7 Activation resulting from a transmural shock of $6.7\ V\ cm^{-1}$ in the rat cardiac sample of figures 3(b) and 4. Panels (a) and (b) show how in a model with cleavage breaks explicitly modeled, virtual sources on the anodal side of the cleavage planes act to rapidly depolarise across the wall. In contrast, panel (c) shows that transmural activation is slower for a model with continuous conductivities. Panel (d) shows, for a set of regularly spaced sample points throughout the volume, the points with activation times less than or

equal to 3 ms. This panel indicates that there are significant and disjoint regions across the wall that are quickly activated following the application of an extracellular shock stimulus.

Fig. 8 A comparison between finite element and finite volume transmembrane potential solutions along the centreline of the rat tissue sample of Fig. 3(b). Solutions are shown at varying grid resolutions and are given for continuous as well as discontinuous models. The continuous and discontinuous results show similar characteristics between the two solution methods. A key result here is that the finite volume results with an artificial cleavage volume more closely resemble the finite element results than with zero cleavage volume. This underscores the importance of the finite volume method developed in this paper with its ability to assign no modelling volume to cleavage breaks.

Fig. 9 Activation times and wavefronts for a bipolar extracellular midwall stimulus. (a) The position of the activation wavefront at selected times in the continuous tissue model. (b) The position of the activation wavefront at selected times in the discontinuous tissue model. (c) The activation times on a set of sample planes through the midwall. Although the activation wavefronts of (a) and (b) resemble one another, the activation times clearly show adjacent regions of discontinuous activation.

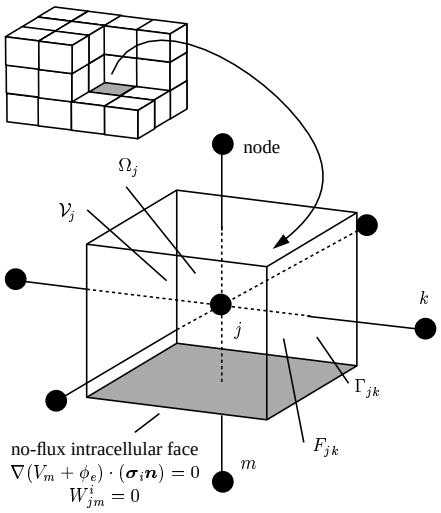

(a) Finite volume definitions.

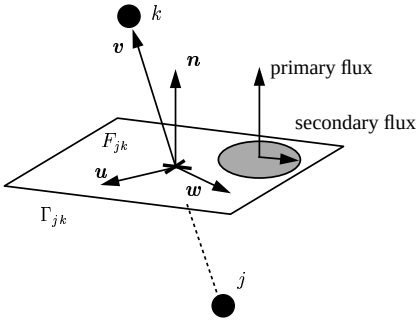

(b) Secondary flux definitions.

Figure 1. Mark Trew ABME

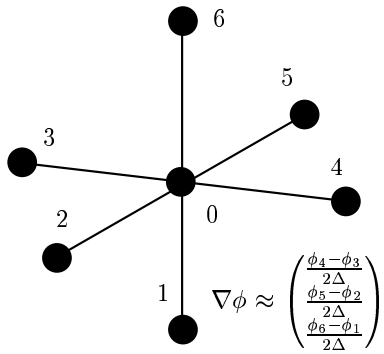

(a) Standard derivative stencil.

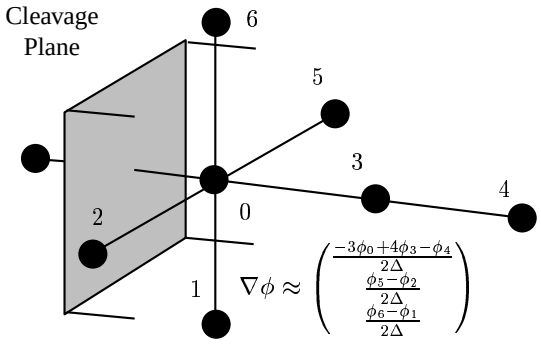

(b) Derivative stencil by cleavage plane.

Figure 2. Mark Trew ABME

Top

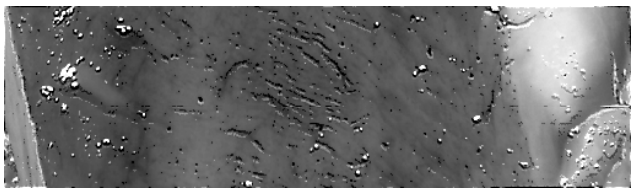

(a) Fresh tissue.

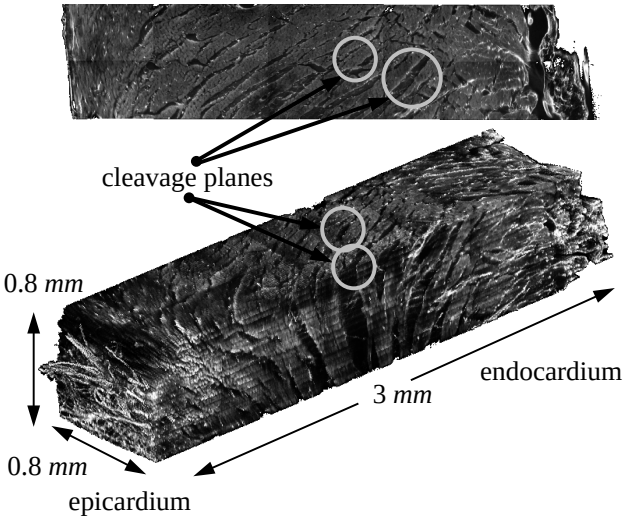

(b) Embedded tissue.

Figure 3. Mark Trew ABME

Top

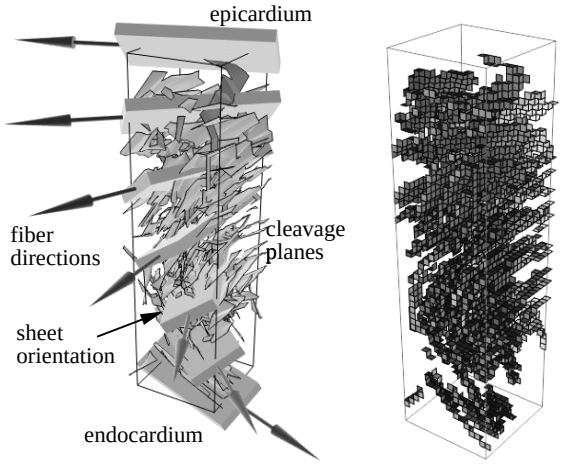

(a) (b)

Figure 4. Mark Trew ABME

Top

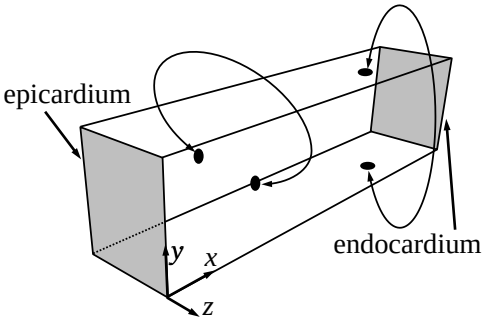

(a) Domain with wrapped boundaries used for shock stimulus modeling.

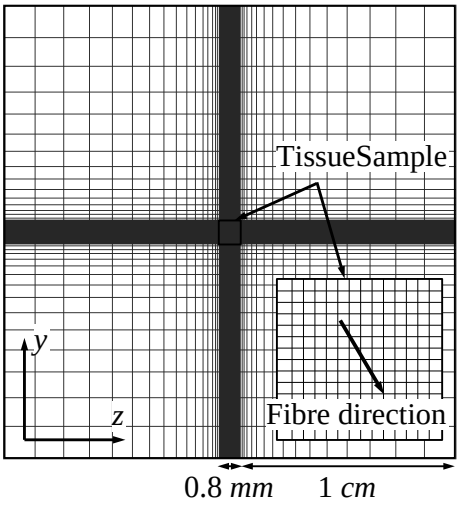

(b) Graded mesh used for bipolar stimulus modeling.

Figure 5. Mark Trew ABME

Top

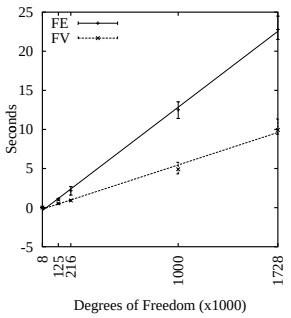

(a) Comparisons of CPU times for linear system solves.

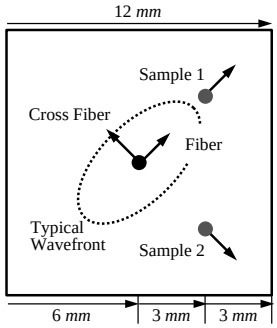

(b) Domain for validation simulations.

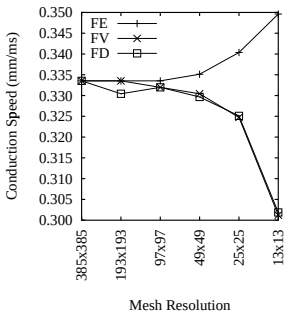

(c) Conduction speed in fiber direction at sample point 1.

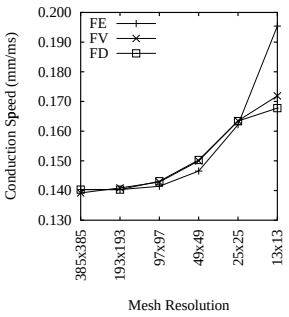

(d) Conduction speed in cross-fiber direction at sample point 2.

Figure 6. Mark Trew ABME

Top

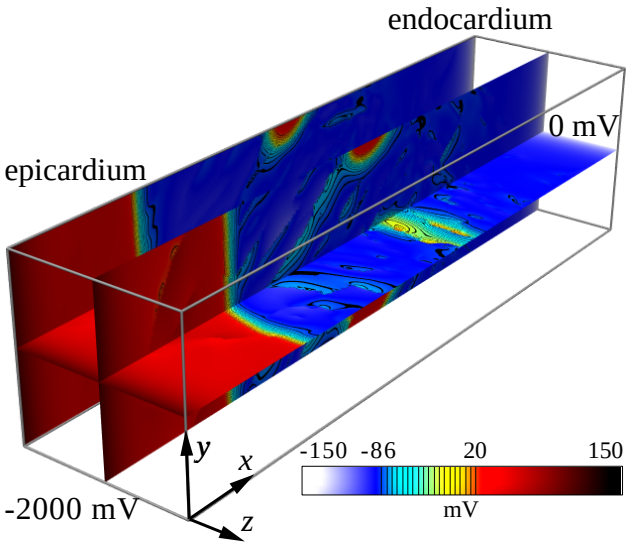

(a) 6.0 ms. Discontinuous model.

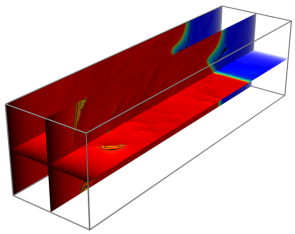

(b) 10.0 ms. Discontinuous model

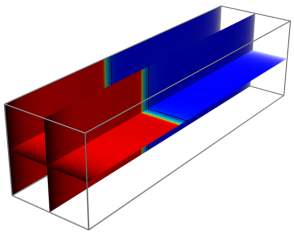

(c) 10.0 ms. Continuous model.

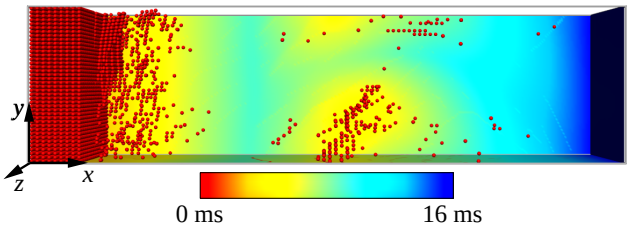

(d) Points with activation times $\leq$ 3.0 ms in discontinuous model.

Figure 7. Mark Trew ABME

Top

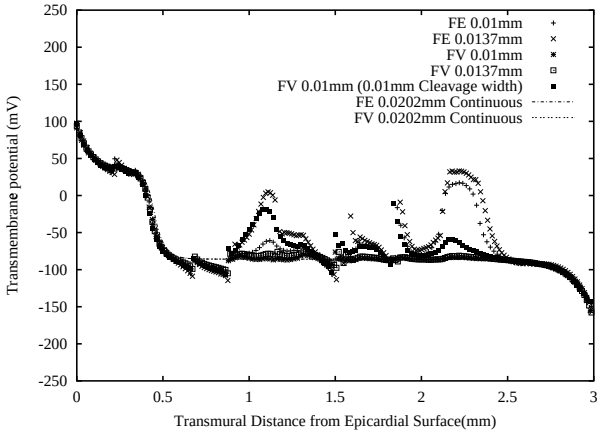

(a) 5 ms

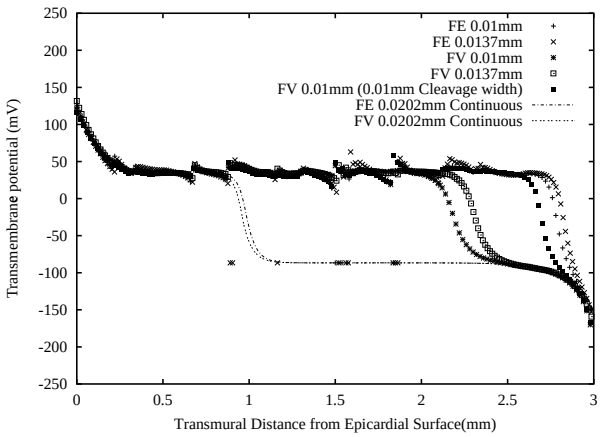

(b) 10 ms

Figure 8. Mark Trew ABME

Top

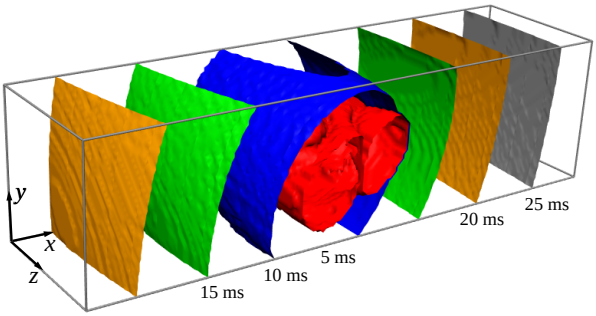

(a) Position of activation wavefront at selected times in continuous model.

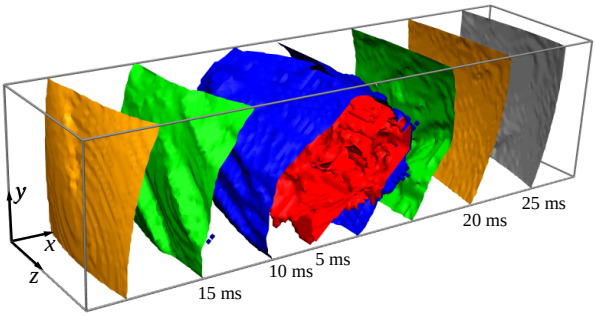

(b) Position of activation wavefront at selected times in discontinuous model.

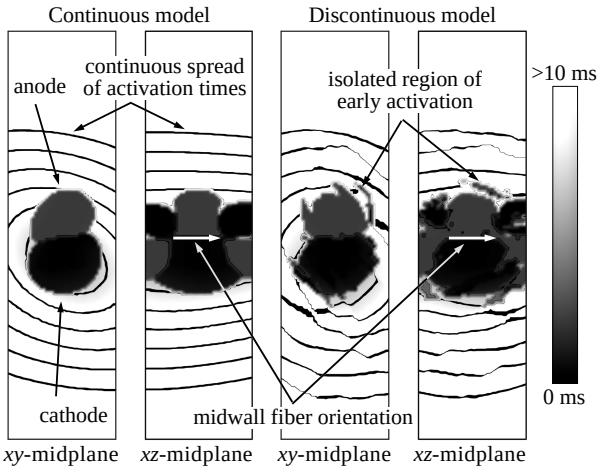

(c) Early and late activation times for continuous and discontinuous models.

Figure 9. Mark Trew ABME